communications materials

ARTICLE

https://doi.org/10.1038/s43246-022-00316-5 OPEN

Strain-tuned topological phase transition and unconventional Zeeman effect in $ZrTe_5$ microcrystals

Apurva Gaikwad[1,8], Song Sun[2,3,8], Peipei Wang[4], Liyuan Zhang[4], Jennifer Cano[1,5✉], Xi Dai[6,7✉] & Xu Du[1✉]

The geometric phase of an electronic wave function, also known as Berry phase, is the fundamental basis of the topological properties in solids. This phase can be tuned by modulating the band structure of a material, providing a way to drive a topological phase transition. However, despite significant efforts in designing and understanding topological materials, it remains still challenging to tune a given material across different topological phases while tracing the impact of the Berry phase on its quantum transport properties. Here, we report these two effects in a magnetotransport study of $ZrTe_5$. By tuning the band structure with uniaxial strain, we use quantum oscillations to directly map a weak-to-strong topological insulator phase transition through a gapless Dirac semimetal phase. Moreover, we demonstrate the impact of the strain-tunable spin-dependent Berry phase on the Zeeman effect through the amplitude of the quantum oscillations. We show that such a spin-dependent Berry phase, largely neglected in solid-state systems, is critical in modeling quantum oscillations in Dirac bands of topological materials.

[1] Department of Physics and Astronomy, Stony Brook University, Stony Brook, NY 11794, USA. [2] Beijing National Laboratory for Condensed Matter Physics, and Institute of Physics, Chinese Academy of Sciences, 100190 Beijing, China. [3] University of Chinese Academy of Sciences, 100049 Beijing, China. [4] Department of Physics, Southern University of Science and Technology, 518055 Shenzhen, China. [5] Center for Computational Quantum Physics, Flatiron Institute, New York, NY 10010, USA. [6] Materials Department, University of California, Santa Barbara, CA 93106-5050, USA. [7] Department of Physics, The Hongkong University of Science and Technology, Clear Water Bay, Kowloon, 999077 Hong Kong, China. [8] These authors contributed equally: Apurva Gaikwad, Song Sun. ✉email: jennifer.cano@stonybrook.edu; daix@ust.hk; xu.du@stonybrook.edu

Topological phase transitions in many materials can be described by a massive Dirac equation at a time reversal invariant momenta. When the energy gap closes and reopens, the mass term in the corresponding Dirac equation changes sign, which can be reflected by the evolution of Berry phase along the Fermi surface if the system is slightly doped[1–6]. Both the evolution of the band gap and the Berry phase can be probed in quantizing magnetic fields, where Shubnikov de Haas (SdH) oscillations from Landau level quantization provides a tool to probe "Fermiology"[7–11]. In addition to Landau level quantization, the Zeeman effect splits the spin-degenerate Landau levels. The difference in the Berry phases between the spin-split Landau levels plays a crucial rule in the SdH oscillations. Interestingly, while the Zeeman effect has been extensively studied over the past decades[12,13], its connection to band topology and non-trivial Berry phase has emerged only recently. A Dirac band with a finite mass gap hosts spin-dependent Berry phase which can modify the SdH oscillations through the Zeeman effect, as recently demonstrated in the spin-zero effect[14,15]. Such a spin-dependent Berry phase is expected to be fundamentally generic for Dirac-like bands, and is band parameter dependent. It is therefore desirable to conduct a comprehensive study of such effect in a system with tunable band parameters.

Despite the significant developments in topological materials study in recent years, it remains a challenge to tune between different topological phases, and correspondingly the Berry phase, in the same material. Strain is a widely proposed mechanism for driving a topological phase transition[16–26]. And transition metal pentatelluride $ZrTe_5$ is a promising material for such study. $ZrTe_5$ is a van der Waals layered material with orthorhombic lattice structure, with layer planes extending along the a- and c- lattice directions and stacking along the b direction. Its electronic properties of is largely dominated by the Fermi surface centered around the Γ point with a Dirac dispersion, but can also have contribution from the parabolic side bands with Fermi surfaces centered between the R and E points in the Brillouin zone (see Supplementary Note 2). $ZrTe_5$ hosts intriguing properties such as a resistance peak (Lifshitz transition)[27–29], chiral magnetic effect[30], and 3D quantum Hall effect[31]. In its 3D bulk form, $ZrTe_5$ has a Dirac-like low energy band structure, with sample-dependent mass gap rendering the material from Dirac semimetal to topological insulator[30,32–36], suggesting extreme sensitivity to lattice deformations. Recently a strain-induced weak topological insulator (WTI) to strong topolgical insulator (STI) transition has been proposed[37,38], followed by experimental evidence in angle-resolved photoemission spectroscopy (ARPES) study[39], and indirect charge transport evidences via the chiral anomaly effect[40]. A charge transport study of the quantum oscillations which directly map the topological phase transition is still lacking. Such bulk transport measurements would be complementary to the surface-sensitive ARPES study, and also reveal the spin-dependent Berry phase over tunable band parameters.

In this work, we study charge transport and SdH oscillations in $ZrTe_5$ under tunable uniaxial strain. In a magnetic field perpendicular to the a–c plane and the applied current, SdH oscillations and their evolution over strain allow direct mapping of the WTI-STI transition through the closing and reopening of the Dirac band mass gap. The dependence of the SdH oscillation amplitude on the Fermi energy and Dirac mass gap, tunable through the strain, is analyzed and compared with the quantum oscillation theory. Our results reveal that the spin-dependent Berry phase intrinsic to the Dirac bands, which has been largely neglected in previous studies, is critical in modeling the SdH oscillations in such topological materials.

Results and discussion

Magnetotransport under tunable strain. The samples studied in this work are $ZrTe_5$ microcrystals mechanically exfoliated onto flexible Polyimide substrates (Fig. 1a–c), which allow application of external tensile and compressive strains along the a-axis through substrate bending, over a wide temperature range from room temperature down to below 4K (see Methods: Sample fabrication and characterization, and Supplementary Note 3). Our $ZrTe_5$ exhibits a strain-tunable resistance peak at $T_p \approx 140$ K(Fig. 1e). At $T = 20$K a non-monotonic resistance versus strain dependence is observed (Fig. 1f), consistent with the report in

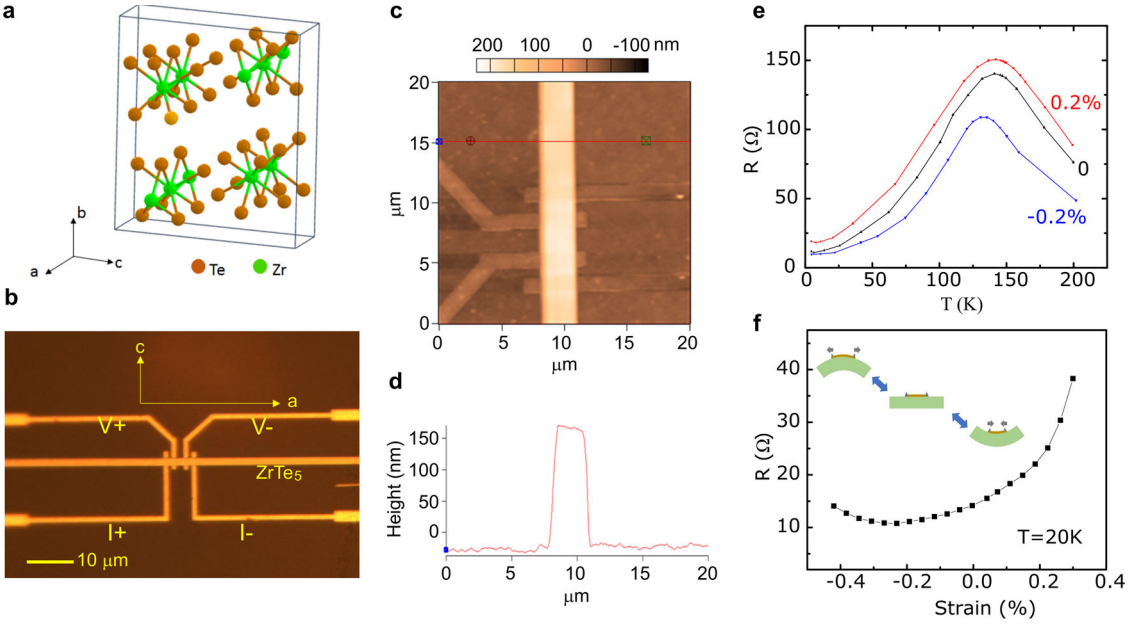

Fig. 1 $ZrTe_5$ under strain. a Crystal structure of $ZrTe_5$. **b** Optical microscope image of $ZrTe_5$ microcrystal on Polyimide substrate with predefined current and voltage electrodes. **c** Atomic force microscope image of the sample. **d** The cross section of the $ZrTe_5$ crystal, with a thickness of ~190 nm. **e** Resistance versus temperature dependence under various external strains. **f** Non-monotonic strain dependence of resistance at the fixed temperature of 20K, showing a resistance minimum at compressive strain ≈ −0.2%. Inset: application of uniaxial strain through substrate bending.

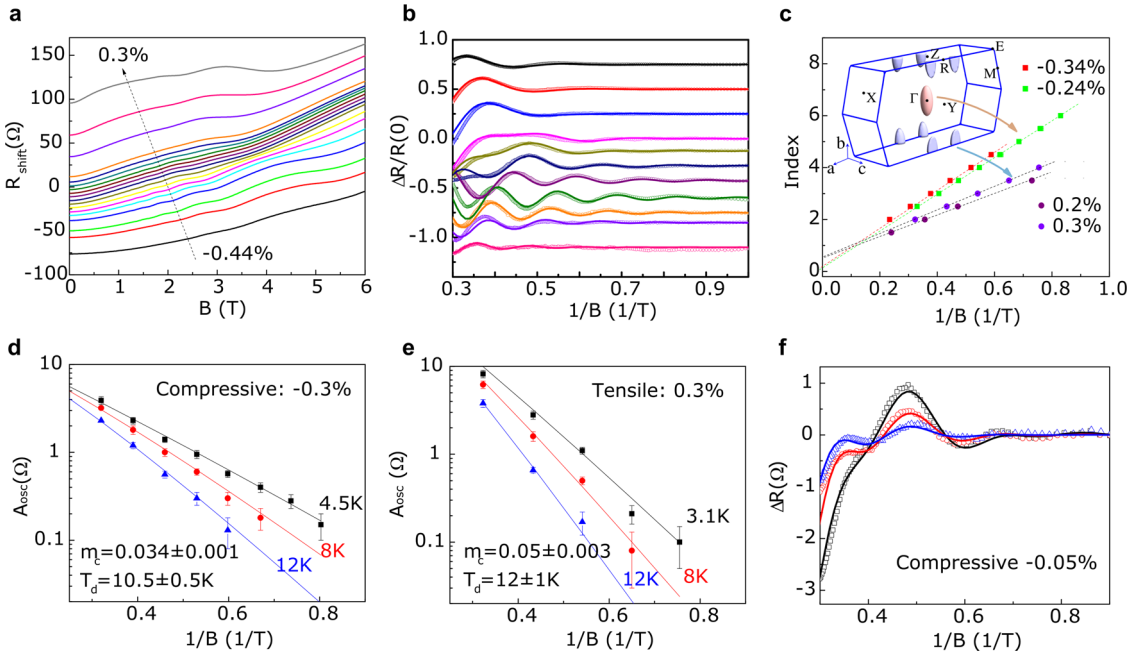

Fig. 2 Magnetotransport measurements on $ZrTe_5$ under strain. a Resistance versus magnetic field in various external strains. The curves are shifted in proportion to the strain for clarity, from the bottom to the top: −0.44, −0.34, −0.3, −0.24, −0.21, −0.19, −0.17, −0.15, −0.13, −0.11, −0.09, −0.07, −0.05, −0.03, 0, 0.1, 0.2, 0.3%. **b** SdH oscillations versus inverse magnetic field in various external strains. The curves ares shifted in proportion to the strain for clarity, from the bottom to the top: −0.44, −0.34, −0.3, −0.24, −0.17, −0.11, −0.05, 0, 0.1, 0.2, 0.3%. Symbols are experimental data and solid lines are simulations using the two-component LK formula. **c** Landau index, obtained from SdH oscillations, versus inverse magnetic field in large compressive and tensile strains (red square: −0.34%, green sqaure: −0.24%, brown circle: 0.2%, blue circle 0.3%). Here resistance peaks and valleys are assigned integer and half integer indices, respectively. The inset show the pockets of Fermi surface, with the Dirac band at the Γ point and a parabolic side band between the R and E points dominating the SdH oscillations under strong compressive and tensile strains, respectively. **d**, **e** SdH amplitude versus inverse magnetic field and temperature in strong compressive (−0.3%) and tensile (0.3%) strains. The symbols are experimental data and the solid lines are fittings using the LK formula. From the fittings, the effective cyclotron mass and Dingle temperature can be obtained. The vertical error bars denote the uncertainty in identifying the SdH oscillation amplitude. **f** Under medium strains the SdH oscillations (open symbols) are directly simulated (solid lines) with the two-component LK formula at various temperatures: black: 3K; red: 8K; and blue: 12K.

macroscopic $ZrTe_5$ crystals[40]. A large strain gauge factor ranging 10^2−10^3 generally presents throughout the temperature range up to room temperature. The gauge factor observed here is very large compared to that of the metal thin films (~2), and is comparable to typical single crystal semiconductors such as Si and Ge (~100). The large gauge factor manifests a strain-sensitive band structure and a small Fermi surface.

Next, we characterize the electrical resistance in magnetic field perpendicular to the a–c crystal plane. At the base temperature of ≈4K, SdH oscillations are clearly visible on the magnetoresistance background and evolve with changing strain (Fig. 2a). Plotting the oscillatory part ΔR versus inverse magnetic field $1/B$, equally spaced resistance oscillations can be resolved (Fig. 2b). In the limits of large compressive and tensile strains applied here, the oscillation amplitude monotonically decreases with increasing $1/B$. Under mild compressive strains, however, the SdH oscillation amplitude appears non-monotonic, suggesting contributions from more than a single Fermi surface.

Analysis of SdH oscillations. Our analysis of the SdH oscillations focuses on mapping out the strain-dependent mass gap, Fermi level, and the spin-dependent Berry phase. We model $ZrTe_5$ by an anisotropic Dirac Hamiltonian (see Methods: Computing the g-factor). Starting from a full Hamiltonian including all the Bloch bands, we divide the Hilbert space into a low energy subspace consisting of the Dirac bands, and a high energy subspace containing all the other bands. When a magnetic field is applied, the vector potential couples the two subspaces and must be downfolded into the low energy bands at the Fermi level, which gives rise to the nonzero g-factor terms in the two-band Dirac model for the low energy subspace, g_p and g_s. We note that such a down folding process includes the contribution to the orbital magnetic moments (the importance of which in the analysis of quantum oscillations has been recently pointed out[11]) from the high energy bands and the contribution from the low energy bands can be captured by the Landau quantization with the Berry curvature being considered[15,41].

In quantizing magnetic fields, the extremal cross-sectional area of the Fermi surface is $S_F = \pi(\mu^2 - \Delta^2)/(\hbar^2 v^2)$. The corresponding cyclotron mass is $m_c = \frac{\hbar^2 \partial S_k}{2\pi \partial \mu} = \frac{\mu}{v^2}$. Here μ is the Fermi energy, Δ is the mass gap, and $v \approx 5 \times 10^5\ \mathrm{m\ s^{-1}}$ is the Dirac band velocity in the a–c plane[32]. The SdH oscillations can be modeled with the Lifshitz–Kosevich (LK) formula: up to the second order in the B field, each single band contributes to the SdH oscillations:

$$\Delta R/R_0 \propto R_D R_T \cos\left(\frac{\hbar S_F}{eB} + \phi_B + \pi + \delta\right) \quad (1)$$

We note that the conventional (parabolic band) LK formula and its Dirac version[42] have the same mathematical form with their corresponding band parameters (see Supplementary Note 5). In Eq. (1) R_0 is the zero magnetic field resistance. Defined for Dirac band, $R_D = \exp(-2\pi^2 k_B T_d |\mu|/\hbar e B v^2)$ is the amplitude reduction factor from disorder scattering, where T_d is the Dingle temperature characterizing the level of disorder,and k_B is the Boltzmann constant. $R_T = \xi/\sinh(\xi)$ is the amplitude reduction

factor from temperature, where $\xi = 2\pi^2 k_B T\mu/\hbar eBv^2$. ϕ_B is the Berry phase, and $\delta = \pm\pi/4$ in 3D materials.

Zeeman effect and spin-dependent Berry phase. Now we consider the Zeeman effect, which splits a spin-degenerate band into two, each with a different Fermi surface extremal cross-sectional area: $S_{F\uparrow/\downarrow} = S_F \pm \alpha B$, and Berry phase: $\phi_{B\uparrow/\downarrow} = \phi_B \pm \phi_s$[15]. Here α describes the splitting of extremal cross-sectional area of the Fermi surface and ϕ_s is the spin-dependent part of the Berry phase. Due to the strong spin-orbit coupling in $ZrTe_5$ spin is not a good quantum number at general momenta: here spin up and spin down refer to "pseudo spins" defined as the two eigenstates of the mirror reflection operator through the $k_z = 0$ plane, which contains the extremum projection of the Fermi surface. The overall quantum oscillation is a summation of the two oscillation terms from the two spin bands: $\cos\left(\frac{\hbar S_{F\uparrow}}{eB} + \phi_{B\uparrow} + \pi + \delta\right) + \cos\left(\frac{\hbar S_{F\downarrow}}{eB} + \phi_{B\downarrow} + \pi + \delta\right) = 2\cos\left(\frac{\hbar S_F}{eB} + \phi_B + \pi + \delta\right)\cos\left(\frac{\hbar\alpha}{e} + \phi_s\right)$ Interestingly S_F and ϕ_B, which are the common (spin-independent) part of the two spin bands before the Zeeman splitting, determines the period and phase offset of the quantum oscillations; while the difference between the two spin bands determines the amplitude.

For systems with non-trivial Berry curvature, the Berry phase splitting ϕ_s along the Fermi surface will be nonzero. In particular, for a Dirac electron system, we find (see Methods: Quantum oscillations)

$$\phi_s = \pi\frac{\Delta}{\mu} \tag{2}$$

$$\begin{aligned}\phi_{B\uparrow} &= \pi + \phi_s = \pi\left(1 + \tfrac{\Delta}{\mu}\right)\\ \phi_{B\downarrow} &= \pi - \phi_s = \pi\left(1 - \tfrac{\Delta}{\mu}\right)\end{aligned} \tag{3}$$

Defining the Zeeman effect-induced SdH amplitude reduction factor: $R_s = \cos\left(\frac{\hbar\alpha}{e} + \phi_s\right)$, we derive for the Dirac band:

$$\Delta R/R_0 = AR_D R_T R_s \cos\left(\frac{\pi(\mu^2 - \Delta^2)}{eB\hbar v^2} + \delta\right), \tag{4}$$

Further, the coefficient α is computed from the g-factor tensor obtained from first-principle calculations at given values of Δ and μ_F.

Under large compressive and large tensile strains, we observed approximately single SdH oscillation frequencies and a monotonic decay of SdH oscillation amplitude over increasing $1/B$, suggesting that SdH oscillations are dominated by single bands there. The linear dependence of the Landau level indices on $1/B$ (Fig. 2c) extrapolates to the index values of close to 0 and 1/2 at $1/B = 0$, corresponding to a SdH oscillation phase change from approximately zero to π. Fitting the $1/B$ and T dependence of the SdH oscillation amplitude to the LK formula (examples shown in Fig. 2d–f) provides estimations to the cyclotron mass and the Dingle temperature at these particular strains.

More generally, the SdH oscillations show a complex $1/B$ dependence which can be modeled considering contributions from two bands: $\Delta R = \Delta R_1 + \Delta R_2$. Here band 1 is a Dirac band (with corresponding Fermi surface centered around the Γ point) with a common Berry phase of π for its two spins bands and hence a overall SdH phase which is much smaller than π (Fig. 2c). Band 2, a "trivial" parabolic band (with corresponding Fermi surface between the R and E points) possess a overall SdH phase which is close to π. We note that evidence of charge transport contribution from a secondary band has been reported previously[28]. The change of SdH phase shown in Fig. 2c is due to the strain-evolution of the relative contribution from the two bands, instead of band topology transition within the same band.

Figure 2b compares the measured SdH oscillations with the two-component LK formula simulations at base temperatures. Here the Dirac band SdH oscillations are modeled with Eq. (4), while the SdH oscillations from the trivial band are modeled with the conventional LK formula, with parameters including T_d, Fermi energy and cyclotron mass m_c. The band parameters used in the simulations are chosen so that they evolve smoothly with changing strain, and yield SdH oscillations which agrees with the experimental observations (with small deviations which may be attributed to the choices of background curves when extracting the oscillatory part of the data). The more general comparisons including temperature dependence are shown in the Supplementary Note 4. Figure 3 plots the key simulation parameters. Here we also include the estimated uncertainties of the parameters beyond which the simulated SdH oscillations deviate noticeably from the measurements. Focusing on the Dirac band, a closing and re-opening of mass gap with tuning external strain happens at a compressive strain of $\approx -0.2\%$. This, remarkably, is a direct transport evidence of the theoretically predicted WTI to STI transition. Associated with such transition, the Fermi energy (measured from the center of the mass gap) shows a non-monotonic strain dependence, reaching a minimum close to the transition strain where mass gap vanishes. From the mass gap and the Fermi energy, we calculate the electron doping: $\mu - \Delta$, which characterizes the energy of the Fermi level in relation to the bottom of the conduction band. The result indicates a maximum electron doping at the WTI-STI transition, which decreases when strain-tuned away from the transition. Generally the analysis of the band parameters suggests a band evolution with strain which is depicted in Fig. 4a.

Compared to the previous (ARPES and chiral magnetic effect) reports on WTI-STI transition, a similar order of magnitude of strain was applied in our studied here ($\approx few - 0.1\%$). The absolute value of the strain at the transition point, however, is randomly shifted by a random built-in stress (typically tensile), resulting from the hot-transfer fabrication process. We note that the observed STI-WTI transition coincides with the minimum resistance point (Fig. 1e), consistent with the previous experimental study on chiral magnetic effect in $ZrTe_5$ under strain[40]. The strain-tunable bandgap observed through our magnetotransport, within the range of strain of a $\approx few - 0.1\%$, varies by a few 10 meV. This is in good agreement with the previous report on ARPES study of $ZrTe_5$ under strain[39].

Next we focus on the impact of Zeeman effect on SdH oscillation amplitude (R_s). Experimentally we obtain R_s at every strain by quantitative simulation of the SdH oscillations. We then compare the results with the theoretical expectation: $R_s = \cos\left(\frac{\hbar\alpha}{e} + \phi_s\right)$. Here $\frac{\hbar\alpha}{e}$, which is associated with the splitting of extremal cross-sectional area of the Fermi surface, follows (see Methods: Quantum oscillations):

$$\frac{\hbar\alpha}{e} = -\pi\frac{\Delta}{\mu} - \pi\frac{\mu}{m_e v^2}\left(\frac{g_z^p}{2}\left(1 + \frac{\Delta}{\mu}\right) - \frac{g_z^s}{2}\left(1 - \frac{\Delta}{\mu}\right)\right) \tag{5}$$

We adopt the g-factors for the s and p orbitals $g_z^p = 9.66, g_z^s = -6.45$, as computed from first-principle calculations (DFT-mBJ)[41]. We note that Eq (5) represents a generalization of the calculation in Ref. [11] by including the effect of higher energy non-Dirac bands, which cause g_p and g_s to deviate from one. ϕ_s, which is associated with the Berry phase splitting along the Fermi surface (Fig. 4b), is calculated from the mass gap and Fermi energy obtained from simulating the SdH oscillations: $\phi_s = \pi\frac{\Delta}{\mu}$. The theory shows good qualitative agreement with the data on the strain dependence of R_s, as

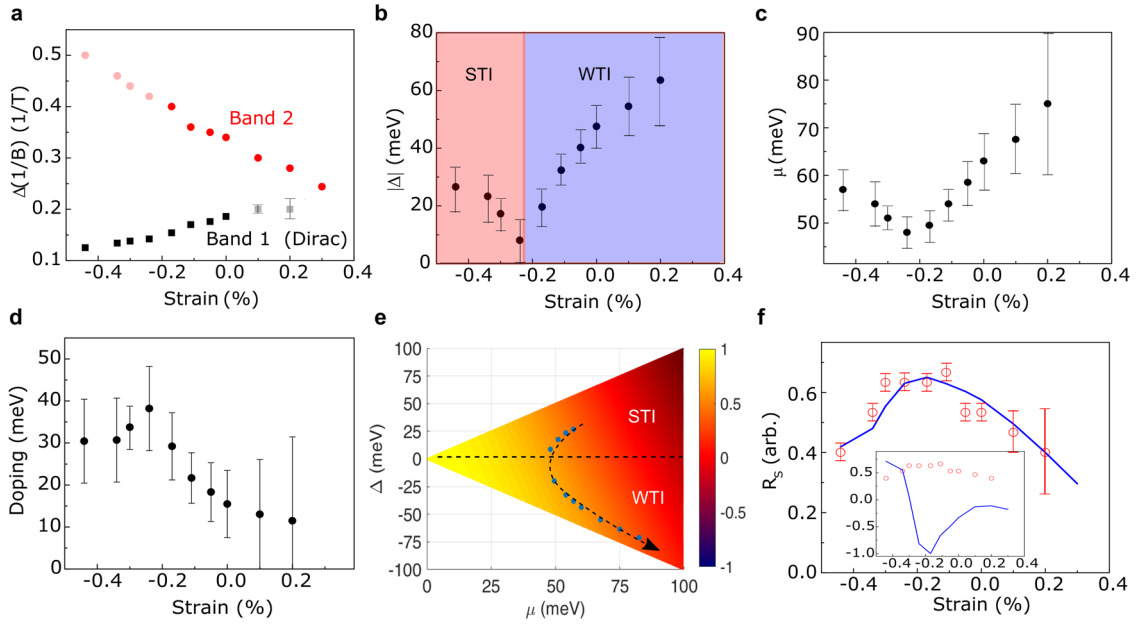

Fig. 3 Strain tuning of band structure and spin-dependent Berry phase. a Strain dependence of SdH oscillation period in inverse magnetic field, for the Dirac band (band 1) and the trivial band (band 2).The results are obtained by simulating the SdH oscillations. The semitransparent data points correspond to when the band has relatively small contribution to the SdH oscillations. The vertical error bars present the interval beyond which the simulated SdH oscillations become noticeably different from the data. For low strains, the error bars are too short to be displayed. The mean values and uncertainties for the other simulation parameters are listed in Supplementary Note 4. **b**, **c** Strain tuning of mass gap size and Fermi energy. The mass gap and the Fermi energy are obtained by simulating the magnetic field and temperature dependence of the SdH oscillation curves with the two-component LK formula. Tuning the external strain from compressive to tensile, the mass gap closes and reopens at around −0.2%, consistent with the STI-WTI topological phase transition. The vertical error bars are determined through standard error propagation. **d** Strain dependence of doping energy, the energy of the Fermi surface counted from the bottom of the conduction band. The vertical error bars are determined through standard error propagation. **e** Theoretical intensity plot of SdH oscillation amplitude reduction factor from Zeeman effect, R_S, as functions of Fermi energy and mass gap. The dotted line shows the boundary between the STI phase (positive mass gap) and the WTI phase (negative mass gap). The symbols in the mass gap-Fermi energy parameter space correspond to the experimental data points at various external strains, evolving following the arrow from compressive to tensile. By convention we assign a negative sign to the mass gap on the WTI side with external strain larger than $\approx -0.2\%$. **f** Theory(solid lines)/experiment(open symbols) comparison of R_S as functions of mass gap and Fermi energy at various strains. The experimental values of R_S are scaled by a common constant factor of 0.6 for comparison with the theory. The theoretical model qualitatively reproduces the experiment results by considering the spin-dependent Berry phase. By contrast, the inset shows the theoretical curve without considering the spin-dependent phase, which fails to explain the experimental data (see Supplementary Note 6). The vertical error bars are determined through standard error propagation.

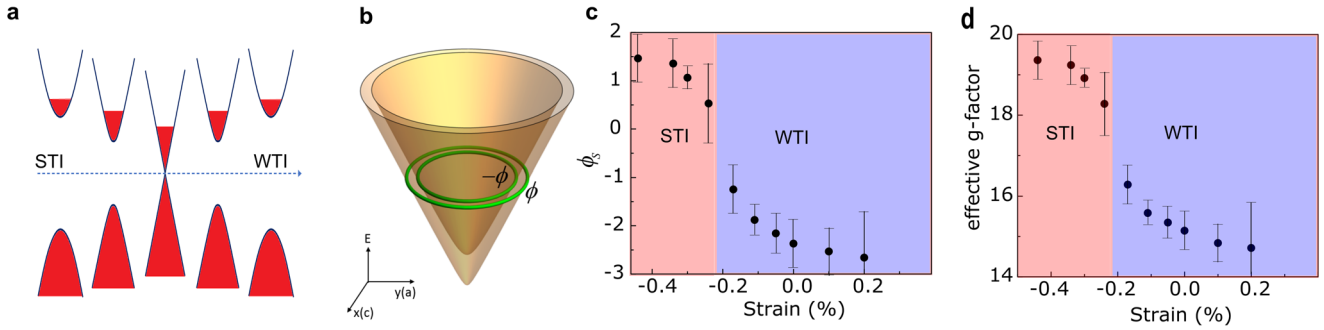

Fig. 4 Evolution of band structure and Zeeman effect over strain. a Evolution of Dirac band and Fermi level through the STI to WTI phase transition with increasingly tensile strain. **b** Schematic energy dispersion with $k_z = 0$ and magnetic field in the z(b) direction. Green circles indicate the boundary of extremal cross-sections for the spin bands. The spin-dependent Berry phases are ϕ and $-\phi$ over the two circles. **c** spin-dependent Berry phase ϕ_s as a function of strain, calculated with mass gap and Fermi energy obtained from the SdH oscillations. **d** Strain tuning of effective g-factor. In both (**c** and **d**), the vertical error bars are determined through standard error propagation.

illustrated in Fig. 3f with the band parameters tuned along the trajectory in the (Δ, μ) parameter space shown in Fig. 3e. By contrast, the conventional modeling of Zeeman effect on SdH oscillations which only considers the Fermi surface splitting (Eq. (5)) completely fails to match with the experimental observations. This comparison definitively highlights the importance of spin-dependent Berry phase in the Zeeman effect. We also note that in our theoretical model, the value of R_S is dependent on both the amplitude and the sign of the energy gap Δ. The quantitative comparison between the theoretical model and our data on R_S, as shown in Fig. 3e and f, therefore reveals a sign-change in band gap near where its

amplitude vanishes. This is consistent with the occurrence of a topological phase transition.

The significant strain-tunability of the spin-dependent Berry phase ϕ_s is shown in Fig. 4c. Accompanied by the topological phase transition where the mass gap vanishes, ϕ_s passes through zero when the system is in the Dirac semimetal phase. We also compute the effective g-factor by comparing R_s with the conventional Zeeman effect-induced SdH amplitude reduction factor $\cos(\pi g m_c/(2m_e))$[7,32]. This leads to $g = 2m_e(\hbar\alpha/e + \phi_s)/(\pi m_c)$, whose strong strain tunability is shown Fig. 4d.

Conclusion

In conclusion, we have carried out a magnetotransport study on the evolution of band topology and non-trvial Berry phase over strain-tunable band parameters in $ZrTe_5$. The strain-dependent SdH oscillations allow direct mapping of the closing and reopening of the Dirac band mass gap, which is consistent with a WTI-STI transition in $ZrTe_5$. Moreover we observed the non-trivial Berry phase and its dependence on band parameters over the transition. Such a spin-dependent Berry phase is generic and intrinsic to Dirac band structure, and is a critical factor in modeling Zeeman effect in SdH oscillations in topological materials.

Methods

Sample fabrication and characterization. The samples studied in this work are $ZrTe_5$ microcrystals mechanically exfoliated onto flexible Polyimide substrates (Fig. 1a, b), which allow application of tensile and compressive strains over a wide temperature range from room temperature down to 4K. $ZrTe_5$ single crystals were synthesized by chemical vapor transport method, with iodine as transport agency. Stoichiometry amounts of Zr(4N) and Te(5N) powder, together with 5mg/mL I_2, were loaded into a quartz tube under argon atmosphere. The quartz tube was flame sealed and then placed in a two-zone furnace, a temperature gradient from 480 °C to 400 °C was applied. After 4 weeks reaction, golden, ribbon-shaped single crystals were obtained, of typical size about $0.6 \times 0.6 \times 5\,mm$. The X-ray diffraction characterization of the crystals is shown in the Supplementary Note 1.

To avoid degradation of the material from ambient exposure, the crystals are exfoliated and press-contacted on predefined gold electrodes on 120 μm-thick Polyimide substrates in Ar environment, and are encapsulated with poly(methyl methacrylate) (PMMA) which both protects the crystals from degradation and facilitates the application of strain. A detailed description on the sample fabrication and on the contact/crystal interface can be found in reference[43]. Uniaxial strain is applied through substrate bending. The strain homogeneity is facilitated by the total emersion of the crystal in PMMA, and more importantly the extremely small ratio of crystal thickness (~190 nm) to the total crystal length (~100 μm, we note that the length of the crystal outside the electrodes also helps creating an uniform strain throughout the thickness of the crystal). All measurements were done with electric current applied along the a-axis. Typical contact resistance over a 10 μm^2 contact area is between few hundred ohms to a few kilo-ohms, and does not change significantly over the application of strain through substrate bending. Uniaxial strain is applied to the samples using a four-point bending setup, with motorized precision control to the substrate curvature[44,45]. Because the substrate is much thicker than the microcrystals, significant uniaxial strain can be achieved at relatively mild substrate curvatures under which the strain on the microcrystals is predominantly tensile/compressive due to the elongation/compression of the top substrate surface where the microcrystals are PMMA-pinned. Besides external strain applied through substrate bending, both the crystals, the substrates, and the encapsulating PMMA layer go through thermal expansion/contraction upon temperature change. Because of such complication it is difficult to precisely characterize the absolute strain on the crystals. Here we focus on the dependence of the transport characteristics on the change of strain induced by substrate bending, which is described in the discussion below as "external strain". In magnetotransport measurements, we limit the temperature range between 3 and 20K, where the change of thermal expansion is small in comparison to the range of the external strain. All charge transport measurements were performed in a Oxford Variable Temperature Insert with a superconducting magnet, using standard lock-in technique.

Computing the *g*-factor. To compute the effect of Zeeman coupling on quantum oscillations, we study the $\mathbf{k}\cdot\mathbf{p}$ Hamiltonian near Γ, which is an anisotropic gapped Dirac Hamiltonian[41]:

$$H(\mathbf{k}) = \begin{pmatrix} \Delta\sigma_0 & \hbar\sum_i v_i k_i \sigma_i \\ \hbar\sum_i v_i k_i \sigma_i & -\Delta\sigma_0 \end{pmatrix}, \tag{6}$$

in the basis $|p,\frac{1}{2}\rangle$, $|p,-\frac{1}{2}\rangle$, $|s,\frac{1}{2}\rangle$, $|s,-\frac{1}{2}\rangle$, where $\pm\frac{1}{2}$ refers to the z-component of spin. In Eq. (6), Δ is half the mass gap; $v_{x,y,z}$ are the anisotropic Dirac cone velocities; $\sigma_{x,y,z}$ are the Pauli matrices; and σ_0 is the 2×2 identity matrix. The eigenvalues of $H(\mathbf{k})$ are

$$E_\pm = \pm\sqrt{\Delta^2 + \hbar^2\sum_i v_i^2 k_i^2}, \tag{7}$$

where all bands are doubly-degenerate due to the combination of time-reversal and inversion symmetry. The eigenvectors are given by

$$\left|\psi^\pm_{m,\mathbf{k}}\right\rangle = \sqrt{\frac{E_\pm+\Delta}{2E_\pm}}\begin{pmatrix} u_m \\ \frac{\hbar v}{E_\pm+\Delta}\mathbf{p}\cdot\boldsymbol{\sigma}u_m \end{pmatrix}, \tag{8}$$

where $u_1 = (1,0)^T$, $u_2 = (0,1)^T$ and we have defined the rescaled coordinates $p_i = v_i k_i / v$.

The Zeeman coupling for the four-band model is:

$$H_0^Z = \mu_B\begin{pmatrix} \sum_i g_i^p B_i & 0 \\ 0 & \sum_i g_i^s B_i \end{pmatrix}, \tag{9}$$

where $g^{s,p}_{x,y,z}$ are the matrix-valued g-factors for the s and p orbitals, which are anisotropic due to the crystal symmetry and which differ from their bare value due to coupling with all the other bands not in the four-band model.

To compute the quantum oscillations, we must downfold this four-band model into the two bands at the Fermi level. We seek an *effective*g-factor for the two degenerate bands that make up the Fermi surface, such that when projected onto those bands, the Zeeman Hamiltonian takes the form:

$$H^Z_{mm'} = \mu_B \mathbf{g}_{mm'}\cdot\mathbf{B}, \tag{10}$$

where $\mu_B = \frac{e\hbar}{2m_e}$ is the Bohr magneton and m, m' index the two bands at the Fermi surface.

The effective g-factor has two contributions:

$$\boldsymbol{g} = \boldsymbol{g}_0 + \boldsymbol{g}_D, \tag{11}$$

where $\boldsymbol{g}_0$ is the projection of g^s and g^p (defined by H_0^Z) onto the two conduction bands at the Fermi level and $\boldsymbol{g}_D$ is an extra orbital contribution that we will describe below. For a magnetic field in the z direction, using the expressions for the conduction band eigenstates from Eq. (8),

$$\boldsymbol{g}_{0,z} = \left(\frac{E_+ + \Delta}{2E_+}\right)\left(g_z^p + g_z^s\frac{\hbar^2v^2(p_z^2 - p_x^2 - p_y^2)}{(E_+ + \Delta)^2}\right)\sigma_z, \tag{12}$$

where the Pauli matrix σ_z acts in the basis of the two bands at the Fermi level. Ultimately, we will only need the g-factor at the extremum of the Fermi surface, where $p_z = 0$ and $\hbar^2v^2(p_x^2 + p_y^2) = \mu^2 - \Delta^2$. In this case,

$$\boldsymbol{g}^{\text{ext}}_{0,z} = \frac{1}{2}\left(g_z^p\left(1 + \frac{1}{\gamma}\right) - g_z^s\left(1 - \frac{1}{\gamma}\right)\right)\sigma_z \tag{13}$$

where $\gamma = \frac{\mu}{\Delta}$ is a dimensionless constant.

Returning to the second term in Eq. (11), $\boldsymbol{g}_D$ is the orbital contribution to the g-factor from the Dirac cone[46]:

$$\mathbf{g}_{D,mm'}(\mathbf{k}) = \frac{im_e}{\hbar^2}\sum_{ijk}\varepsilon_{ijk}\hat{\mathbf{e}}_k\left\langle\partial_i\psi_{m,\mathbf{k}}\right|\left(H(\boldsymbol{k}) - E_{m,\mathbf{k}}\right)\left|\partial_j\psi_{m',\mathbf{k}}\right\rangle, \tag{14}$$

where $\psi_{m,\mathbf{k}}$ are the eigenvectors of Eq. (6).

The first step to evaluate $\boldsymbol{g}_D$ is to find the derivatives of the eigenstates:

$$\frac{\partial\left|\psi_{m,\mathbf{k}}\right\rangle}{\partial p_i} = \sqrt{\frac{E+\Delta}{2E}}\begin{pmatrix} -\frac{\Delta\hbar^2v^2p_i}{2E^2(E+\Delta)}u_m \\ -\frac{(\Delta+2E)\hbar^3v^3p_i}{(E+\Delta)^2 2E^2}\mathbf{p}\cdot\boldsymbol{\sigma}u_m + \frac{\hbar v}{E+\Delta}\sigma_i u_m \end{pmatrix}, \tag{15}$$

where we have dropped the subscript/superscript ± on E and ψ to reduce clutter. After some algebra, it follows that:

$$\left(H - E_{m,\mathbf{k}}\right)\frac{\partial\left|\psi_{m,\mathbf{k}}\right\rangle}{\partial p_i} = \sqrt{\frac{E+\Delta}{2E}}\frac{1}{E(E+\Delta)}\begin{pmatrix} \Delta\hbar^2v^2p_iu_m + iE\hbar^2v^2\sum_{jk}\varepsilon_{jik}p_j\sigma_k u_m \\ \hbar^3v^3p_i\mathbf{p}\cdot\boldsymbol{\sigma}u_m - E(E+\Delta)\hbar v\sigma_i u_m \end{pmatrix}, \tag{16}$$

which yields the matrix element

$$\left\langle\frac{\partial\psi_{m,\mathbf{k}}}{\partial p_i}\right|H(\mathbf{k}) - E_{m,\mathbf{k}}\left|\frac{\partial\psi_{m',\mathbf{k}}}{\partial p_j}\right\rangle = \frac{\hbar^2v^2}{2E^2}u_m^\dagger\left[\frac{-i\hbar^2v^2\varepsilon_{jkl}p_ip_k\sigma_l + i\hbar^2v^2\varepsilon_{ikl}p_jp_k\sigma_l}{E+\Delta} - iE\varepsilon_{ijk}\sigma_k + \frac{\hbar^2v^2p_ip_j}{E} - E\delta_{ij}\right]u_{m'} \tag{17}$$

The terms symmetric under the exchange of the i and j indices (i.e., the last two terms) will cancel in the sum in Eq. (14). Thus, applying Eq. (14), the extra orbital

contribution to the g-factor is given by:

$$\boldsymbol{g}_D = \frac{g^L}{2\tilde{\gamma}^2}\sum_{ijk}\left[\tilde{\gamma}\varepsilon_{ijk}\varepsilon_{ijk}\sigma_k - \frac{2\hbar^2 v^2/\Delta^2}{1+\tilde{\gamma}}\sum_{qr}\varepsilon_{iqr}\varepsilon_{ijk}p_q p_j \sigma_r\right]\frac{v_i v_j}{v^2}\hat{\boldsymbol{e}}_k \tag{18}$$

where $g^L \equiv \frac{m_e v^2}{\Delta}$ and $\tilde{\gamma} \equiv \frac{E}{\Delta}$ are dimensionless constants.

We now simplify this result by taking B in the z-direction and restricting to the boundary of the extremal cross-section, where $p_z = 0$ and $\hbar^2 v^2(p_x^2 + p_y^2) = \mu^2 - \Delta^2$. Plugging this into Eq. (18), we obtain the z-component of $\boldsymbol{g}$:

$$\boldsymbol{g}^{\text{ext}}_{D,z} = \frac{g^L}{\tilde{\gamma}^2}\frac{v_x v_y}{v^2}\sigma_z \tag{19}$$

The total effective g-factor at the extremal cross-section of the Fermi surface is found by combining Eqs. (13) and (19):

$$\boldsymbol{g}^{\text{ext}}_z = \left[\frac{m_e \Delta v_x v_y}{\mu^2} + \frac{g^p_z}{2}\left(1+\frac{\Delta}{\mu}\right) - \frac{g^s_z}{2}\left(1-\frac{\Delta}{\mu}\right)\right]\sigma_z \tag{20}$$

This expression shows that the g-factor in the $\hat{z}$-direction is independent of momentum on the boundary of the extremal cross-section and is diagonal, i.e., $|\psi_{m,\boldsymbol{k}}\rangle$ are eigenstates of the Zeeman coupling.

Quantum oscillations. We now discuss the quantum oscillations of the anisotropic Dirac semi-metal. As discussed in the main text, the quantum oscillations for a doubly degenerate electronlike Fermi surface are proportional to

$$\Delta R/R_0 \propto \cos\left(\frac{\hbar S_F}{eB} + \phi_B + \pi + \delta\right)\cos\left(\frac{\hbar\alpha}{e} + \phi_s\right) \tag{21}$$

where $\phi_{B,\uparrow/\downarrow} = \phi_B \pm \phi_s$ are the Berry phases around the extremal Fermi surface for each of the two spins and $S_{F,\uparrow/\downarrow} = S_F \pm \alpha B$ are the extremal areas of the Fermi surface for each spin.

The Berry connection is defined by[46]: $\boldsymbol{A}_{mm'}(\boldsymbol{k}) = \sum_k i\langle\psi_{m,\boldsymbol{k}}|\frac{\partial}{\partial k_i}|\psi_{m',\boldsymbol{k}}\rangle\boldsymbol{e}_k$. By plugging in the expressions for the eigenstates and derivatives of eigenstates in Eqs. (8) and (15), we find the explicit expression:

$$\begin{aligned}\boldsymbol{A}(\boldsymbol{k}) = \frac{\hbar^2 v}{\Delta^2}\frac{1}{2\tilde{\gamma}(\tilde{\gamma}+1)}\big[&(p_y\sigma_z - p_z\sigma_y)v_x\boldsymbol{e}_x + \\ &(p_z\sigma_x - p_x\sigma_z)v_y\boldsymbol{e}_y + (p_x\sigma_y - p_y\sigma_x)v_z\boldsymbol{e}_z\big]\end{aligned} \tag{22}$$

To find the Berry phase, we ultimately need $\boldsymbol{A}(\boldsymbol{k})\cdot \mathrm{d}\boldsymbol{k}$ on the extremal cross-section, where $p_z = 0$ and $\mathrm{d}\boldsymbol{k}$ is in the x–y plane, which yields:

$$\boldsymbol{A}(\boldsymbol{k})\cdot \mathrm{d}\boldsymbol{k} = \frac{\hbar^2 v_x v_y}{\Delta^2}\frac{\sigma_z}{2\tilde{\gamma}(\tilde{\gamma}+1)}\left(k_y\boldsymbol{e}_x - k_x\boldsymbol{e}_y\right)\cdot \mathrm{d}\boldsymbol{k}, \tag{23}$$

where σ_z is acting in the space of the two conduction bands at the Fermi level. We find the Berry phase around each extremal ring of the Fermi surface by integrating over the the boundary of the extremal cross-section:

$$\oint \boldsymbol{A}(\boldsymbol{k})\cdot \mathrm{d}\boldsymbol{k} = \frac{\hbar^2 v_x v_y}{2\Delta^2\tilde{\gamma}(\tilde{\gamma}+1)}\oint\left(k_y\boldsymbol{e}_x - k_x\boldsymbol{e}_y\right)\cdot \mathrm{d}\boldsymbol{k} \tag{24}$$

The loop integral can be turned into an area integral using Stokes theorem:

$$\iint \nabla_{\boldsymbol{k}}\times\left(k_y\boldsymbol{e}_x - k_x\boldsymbol{e}_y\right)\cdot \mathrm{d}\boldsymbol{S}_{\boldsymbol{k}} = -2\iint dS_{\mathbf{k}} \tag{25}$$

$$= -2\pi\frac{\mu^2 - \Delta^2}{v_y v_x}, \tag{26}$$

which yields:

$$\phi_{B,\uparrow/\downarrow} = \pi\left(1 \pm \frac{\Delta}{\mu}\right), \tag{27}$$

where we have added 2π in order to ensure the Berry phase in the range of 0 to 2π.

The last term that we need to evaluate the Lifschitz-Kosevich formula is the area of the extremal Fermi surfaces. Since the effective g-factor at the extremal Fermi surfaces (Eq. (20)) is diagonal in the basis of the two conduction bands, the two extremal Fermi surfaces satisfy the equation:

$$\mu = \sqrt{\Delta^2 + \hbar^2 v_x^2 k_x^2 + \hbar^2 v_y^2 k_y^2} \pm \mu_B \boldsymbol{g}^{\text{ext}}_z B, \tag{28}$$

accounting for the fact that the magnetic field is in the z direction and the extremal Fermi surfaces have $p_z = 0$. Thus, each extremal cross-section forms an ellipse whose area is given by:

$$S = \frac{\pi}{\hbar^2 v_x v_y}\left[\left(\mu \mp \mu_B \boldsymbol{g}^{\text{ext}}_z B\right)^2 - \Delta^2\right] \tag{29}$$

Thus, the area-splitting term α in Eq. (21) is given by:

$$\alpha = -\frac{\pi e \mu \boldsymbol{g}^{\text{ext}}_z}{\hbar m_e v_x v_y}, \tag{30}$$

where we have used $\mu_B = e\hbar/2m_e$. Plugging in the result for $\boldsymbol{g}^{\text{ext}}_z$ from Eq. (20),

$$\frac{\hbar\alpha}{e} = -\frac{\pi\Delta}{\mu} - \frac{\pi\mu}{m_e v_x v_y}\left[\frac{g^p_z}{2}\left(1+\frac{\Delta}{\mu}\right) - \frac{g^s_z}{2}\left(1-\frac{\Delta}{\mu}\right)\right] \tag{31}$$

Plugging in the calculation of the Berry phase (Eq. (27)) and the area difference (Eq. (31)) to the Lifschitz-Kosevich formula (Eq. (21)), we derive the expression for quantum oscillations:

$$\Delta\rho \propto \cos\left(\frac{\pi\mu}{m_e v_x v_y}\left[\frac{g^p_z}{2}\left(1+\frac{\Delta}{\mu}\right) - \frac{g^s_z}{2}\left(1-\frac{\Delta}{\mu}\right)\right]\right)\cos\left(\frac{\hbar S_F}{eB} \pm \frac{\pi}{4}\right) \tag{32}$$

Data availability

The data that support the findings of this study are available from the corresponding author upon reasonable request.

Code availability

The code that support the findings of this study are available from the corresponding author upon reasonable request.

Received: 24 May 2022; Accepted: 8 November 2022;
Published online: 27 November 2022

References

1. Kane, C. L. & Mele, E. J. Quantum spin hall effect in graphene. *Phys. Rev. Lett.* **95**, 226801 (2005).
2. Kane, C. L. & Mele, E. J. Z_2 topological order and the quantum spin hall effect. *Phys. Rev. Lett.* **95**, 146802 (2005).
3. Andrei, B. B., Taylor, L. H. & Zhang, S.-C. Quantum spin hall effect and topological phase transition in HgTe quantum wells. *Science* **314**, 1757–1761 (2006).
4. König, M. et al. Quantum spin hall insulator state in HgTe quantum wells. *Science* **318**, 766–770 (2007).
5. Moore, J. E. & Balents, L. Topological invariants of time-reversal-invariant band structures. *Phys. Rev. B* **75**, 121306 (2007).
6. Xu, S.-Y. et al. Observation of a topological crystalline insulator phase and topological phase transition in $Pb_{1-x}Sn_xTe$. *Nat. Commun.* **3**, 1192 (2012).
7. Shoenberg, D. *Magnetic Oscillations in Metals*. Cambridge Monographs on Physics. (Cambridge University Press, 1984).
8. Mikitik, G. P. & Sharlai, Y. V. Manifestation of berry's phase in metal physics. *Phys. Rev. Lett.* **82**, 2147–2150 (1999).
9. Novoselov, K. S. et al. Two-dimensional gas of massless dirac fermions in graphene. *Nature* **438**, 197–200 (2005).
10. Zhang, Y., Tan, Y.-W., Stormer, H. L. & Kim, P. Experimental observation of the quantum hall effect and berry's phase in graphene. *Nature* **438**, 201–204 (2005).
11. Alexandradinata, A., Wang, C., Duan, W. & Glazman, L. Revealing the Topology of Fermi-Surface Wave Functions from Magnetic Quantum Oscillations. *Phys. Rev. X* **8**, 011027 (2018).
12. Luttinger, J. M. & Kohn, W. Motion of Electrons and Holes in Perturbed Periodic Fields. *Phys. Rev.* **97**, 869–883 (1955).
13. Cohen, M. H. & Blount, E. I. The g-factor and de haas-van alphen effect of electrons in bismuth. *Philos. Magazine* **5**, 115–126 (1960).
14. Wang, J. et al. Vanishing quantum oscillations in Dirac semimetal $ZrTe_5$. *PNAS* **115**, 9145–9150 (2018).
15. Sun, S., Song, Z., Weng, H. & Dai, X. Topological metals induced by the zeeman effect. *Phys. Rev. B* **101**, 125118 (2020).
16. Lin, C. et al. Visualization of the strain-induced topological phase transition in a quasi-one-dimensional superconductor TaSe3. *Nat. Mater.* **20**, 1093–1099 (2021).
17. Nie, S. et al. Topological phases in the $TaSe_3$ compound. *Phys. Rev. B* **98**, 125143 (2018).
18. Liu, Y. et al. Tuning Dirac states by strain in the topological insulator Bi2Se3. *Nat. Phys.* **10**, 294–299 (2014).
19. Young, S. et al. Theoretical investigation of the evolution of the topological phase of Bi_2Se_3 under mechanical strain. *Phys. Rev. B* **84**, 085106 (2011).
20. Liu, W. et al. Anisotropic interactions and strain-induced topological phase transition in Sb_2Se_3 and Bi_2Se_3. *Phys. Rev. B* **84**, 245105 (2011).

21. Xi, X. et al. Bulk Signatures of Pressure-Induced Band Inversion and Topological Phase Transitions in $Pb_{1-x}Sn_xSe$. *Phys. Rev. Lett.* **113**, 096401 (2014).
22. Ohmura, A. et al. Pressure-induced topological phase transition in the polar semiconductor BiTeBr. *Phys. Rev. B* **95**, 125203 (2017).
23. Zhao, L., Wang, J., Gu, B.-L. & Duan, W. Tuning surface Dirac valleys by strain in topological crystalline insulators. *Phys. Rev. B* **91**, 195320 (2015).
24. Barone, P. et al. Pressure-induced topological phase transitions in rocksalt chalcogenides. *Phys. Rev. B* **88**, 045207 (2013).
25. Juneja, R., Shinde, R. & Singh, A. K. Pressure-Induced Topological Phase Transitions in $CdGeSb_2$ and CdSnSb2. *J. Phys. Chem.* **9**, 2202–2207 (2018).
26. Sadhukhan, S., Sadhukhan, B. & Kanungo, S. Pressure driven topological phase transition in chalcopyrite $ZnGeSb_2$. *arxiv.2201.02347* (2022).
27. Zhang, Y. et al. Electronic evidence of temperature-induced lifshitz transition and topological nature in $ZrTe_5$. *Nat. Commun.* **8**, 15512 (2017).
28. Chi, H. et al. Lifshitz transition mediated electronic transport anomaly in bulk ZrTe5. *New J. Phys.* **19**, 015005 (2017).
29. Morice, C., Lettl, E., Kopp, T. & Kampf, A. P. Optical conductivity and resistivity in a four-band model for $ZrTe_5$ from ab initio calculations. *Phys. Rev. B* **102**, 155138 (2020).
30. Li, Q. et al. Chiral magnetic effect in $ZrTe_5$. *Nat. Phys.* **12**, 550–554 (2016).
31. Tang, F. et al. Three-dimensional quantum hall effect and metal–insulator transition in $ZrTe_5$. *Nature* **569**, 537–541 (2019).
32. Liu, Y. et al. Zeeman splitting and dynamical mass generation in dirac semimetal $ZrTe_5$. *Nat. Commun.* **7**, 12516 (2016).
33. Chen, Z.-G. et al. Spectroscopic evidence for bulk-band inversion and three-dimensional massive dirac fermions in $ZrTe_5$. *PNAS* **114**, 816–821 (2017).
34. Jiang, Y. et al. Landau-level spectroscopy of massive dirac fermions in single-crystalline $zrte_5$ thin flakes. *Phys. Rev. B* **96**, 041101 (2017).
35. Xu, B. et al. Temperature-driven topological phase transition and intermediate dirac semimetal phase in $zrte_5$. *Phys. Rev. Lett.* **121**, 187401 (2018).
36. Xiong, H. et al. Three-dimensional nature of the band structure of $zrte_5$ measured by high-momentum-resolution photoemission spectroscopy. *Phys. Rev. B* **95**, 195119 (2017).
37. Weng, H., Dai, X. & Fang, Z. Transition-metal pentatelluride $ZrTe_5$ and $HfTe_5$: A paradigm for large-gap quantum spin hall insulators. *Phys. Rev. X* **4**, 011002 (2014).
38. Fan, Z., Liang, Q.-F., Chen, Y. B., Yao, S.-H. & Zhou, J. Transition between strong and weak topological insulator in $ZrTe_5$ and $HfTe_5$. *Sci. Rep.* **7**, 45667 (2017).
39. Zhang, P. et al. Observation and control of the weak topological insulator state in $ZrTe_5$. *Nat. Commun.* **12**, 406 (2021).
40. Mutch, J. et al. Evidence for a strain-tuned topological phase transition in $ZrTe_5$. *Sci. Adv.* **5** https://doi.org/10.1126/sciadv.aav9771 (2019).
41. Song, Z. et al. First Principle Calculation of the Effective Zeeman's Couplings in Topological Materials. In *Memorial Volume for Shoucheng Zhang*, Ch. 11, 263–281 (World Scientific, 2021).
42. Gusynin, V. P. & Sharapov, S. G. Magnetic oscillations in planar systems with the dirac-like spectrum of quasiparticle excitations. ii. transport properties. *Phys. Rev. B* **71**, 125124 (2005).
43. Mills, S. et al. Contact transparency in mechanically assembled 2d material devices. *J. Phys: Mater.* **2**, 035003 (2019).
44. Guan, F., Kumaravadivel, P., Averin, D. V. & Du, X. Tuning strain in flexible graphene nanoelectromechanical resonators. *Appl. Phys. Lett.* **107**, 193102 (2015).
45. Guan, F. & Du, X. Random gauge field scattering in monolayer graphene. *Nano Lett.* **17**, 7009–7014 (2017).
46. Xiao, D., Chang, M.-C. & Niu, Q. Berry phase effects on electronic properties. *Rev. Mod. Phys.* **82**, 1959–2007 (2010).

Acknowledgements

X.D. acknowledges support from the National Science Foundation (NSF) under award DMR-1808491. X.D. and J.C. thank Aris Alexandradinata for insightful discussions. J.C. acknowledges the support of the Flatiron Institute, a division of Simons Foundation, and support from the National Science Foundation under Grant No. DMR-1942447.

Author contributions

A.G. and X.D. fabricated the samples and performed the measurements. S.S., J.C., and X.D. formulated the theory. P.W. and L.Z. synthesized the $ZrTe_5$ single crystals. X.D. performed the data analysis and designed the experiment. S.S., J.C., X.D., and Xu.D. wrote the paper.

Competing interests

The authors declare no competing interests.

Additional information

Supplementary information The online version contains supplementary material available at https://doi.org/10.1038/s43246-022-00316-5.

Correspondence and requests for materials should be addressed to Jennifer Cano, Xi Dai or Xu Du.

Peer review information *Communications Materials* thanks Ryo Noguchi, Jian Zhou and the other, anonymous, reviewer(s) for their contribution to the peer review of this work. Primary Handling Editors: Toru Hirahara and Aldo Isidori. Peer reviewer reports are available.

Reprints and permission information is available at http://www.nature.com/reprints

Publisher's note Springer Nature remains neutral with regard to jurisdictional claims in published maps and institutional affiliations.